Turbulent drag reduction by constant near-wall forcing

JIN XU†, SUCHUAN DONG‡, MARTIN R. MAXEY¶
AND GEORGE E. KARNIADAKIS

Division of Applied Mathematics, Brown University, Providence, RI 02912, USA

Computational experiments based on the direct numerical simulation of turbulent channel flow reveal that the skin friction can be reduced as much as 70 % by the action of a localized steady force acting against the flow close to the wall. In addition, the excessive shear stresses observed during the laminar-to-turbulence transition can be substantially reduced. For a sustained reduction in the skin friction, the control force has to act within a distance of 20 wall units (scaling with the location of the maximum Reynolds stress gradient); otherwise a transient drag reduction is observed or even an increase in drag. The forcing leads to the formation of a shear layer close to the wall that reduces the skin friction and limits the development of the Reynolds shear stresses. As the amplitude of the forcing is increased, the shear layer breaks down and generates its own turbulence, setting an upper limit to the level of drag reduction. This transition of the shear layer is correlated with a Reynolds number based on the forcing amplitude and length scale.

1. Introduction

The quest for 'taming' turbulence with the objective of reducing the skin friction on air- and sea-vehicles as well as in gas- and liquid-carrying pipes has been pursued for more than a century. This has led to many proposals for drag-reduction techniques including microgrooves, polymer and microbubble injection, and electromagnetic and acoustic excitation (see Bushnell & Moore 1991; Gad-El-Hak 2000). The use of microgrooves or riblets mounted on the wall surface has proved to be effective in partially suppressing turbulence and reducing skin friction by about 5 % to 10 % (see Bechert & Bartenwerfer 1989; Choi 1989). Transverse oscillations and travelling waves, induced mechanically or electromagnetically, can lead to turbulent drag reduction of about 50 % (as reported by Berger *et al.* 2000; Du & Karniadakis 2000; Karniadakis & Choi 2003). Injection of high molecular weight polymer solutions or gas in the near-wall region of a liquid boundary layer can result in turbulent drag reduction of more than 70 % (see Phillips, Castano & Stace 1998; Deutsch *et al.* 2003; Ptasinski *et al.* 2003).

Closed-loop active control of turbulence has also been successful in reducing turbu-lent drag, but requires system sensors and actuators for implementation. A theoretical

† Present address: Physics Division, Argonne National Lab, Argonne, IL 60439, USA.
‡ Present address: Center for Computational and Applied Mathematics, Department of Mathematics, Purdue University, West Lafayette, IN 47907, USA.
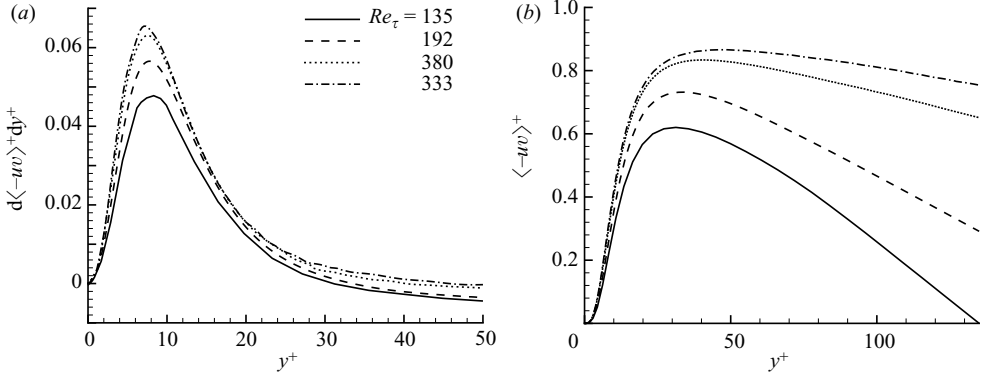¶ Author to whom correspondence should be addressed: maxey@dam.brown.edu

FIGURE 1. Profiles of (*a*) the gradient of the Reynolds shear stress, scaled by u_τ^3/ν and (*b*) Reynolds shear stress, against distance from the wall y^+. Results at $Re_\tau = 135$ (solid line); $Re_\tau = 192$ (dashed line); $Re_\tau = 380$ (dotted line); $Re_\tau = 633$ (dashed-dotted line).

example is provided by the technique of 'opposition control' proposed by Choi, Moin & Kim (1994) and Hammond, Bewley & Moin (1998). Opposition control employs a sensor plane located at a distance from the wall $y^+ = 10$–25, in terms of wall variables, where the wall normal velocity is measured. Opposing inflow/outflow velocity boundary conditions are imposed at the wall so as to give an effective zero wall normal velocity at each point in the sensing plane. The level of drag reduction is about 26 % at $Re_\tau = 100$, but drops to 19 % at $Re_\tau = 720$, as reported by Chang, Collis & Ramakrishnan (2002); further results are given by Iwamoto, Suzuki & Kasagi (2002). The level of drag reduction is also sensitive to the location of the control plane. Another numerical example of flow control is given by Jiménez & Pinelli (1999) where selective filtering of the vorticity transport, averaged in the streamwise direction, leads to a reduction of the near-wall streaks.

In this paper, we consider the effects of a localized constant streamwise forcing applied to the flow. The forcing $\boldsymbol{F}$ is applied in the near-wall region and acts to oppose the flow. The forcing is uniform in directions parallel to the wall. One motivation for this study is a consideration of the effect of the Reynolds shear stress on the mean momentum distribution. For turbulent Poiseuille flow in a channel, the mean momentum equation is

$$\rho \frac{\partial U_1}{\partial t} = -\frac{dP}{dx_1} + \frac{\partial}{\partial x_2}\left\{ -\rho\overline{u_1 u_2} + \mu\frac{\partial U_1}{\partial x_2} \right\} + F_1, \qquad (1.1)$$

and under conditions of steady flow, without forcing, this gives the usual linear shear stress profile, where the sum of the Reynolds stress and viscous stress varies linearly across the channel. The Reynolds stress is zero at the wall and attains a maximum value at a distance from the wall that in terms of wall variables scales with $Re_\tau^{1/2}$ (see Sreenivasan 1989). The acceleration of the mean flow, or the response to an applied forcing F_1, however, depends on the gradient of the shear stress. The gradient of the Reynolds stress is positive near the wall and then has a smaller negative value in the core of the channel. This is illustrated by the simulation results described below and shown in figure 1. Here, the profile of the gradient of the Reynolds shear stress is plotted, scaled in wall variables, for different Reynolds numbers Re_τ. In all cases,
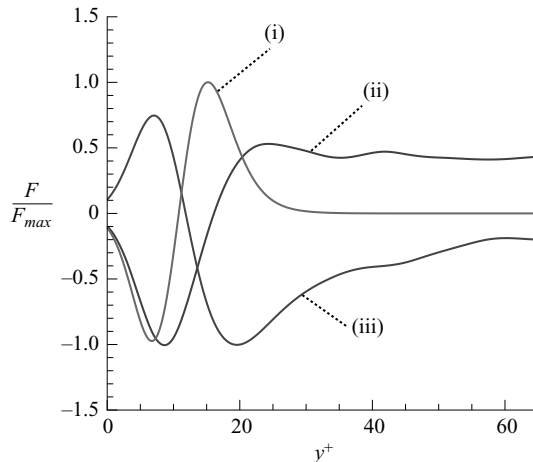
FIGURE 2. Profiles of the average streamwise force density for bubbles and particles in a channel flow at $Re_\tau = 135$ and 200. (i) $Re_\tau = 200$, bubbles; (ii) 135, bubbles; (iii) 135, particles.

the gradient has a maximum at approximately $y^+ = 8$, while the location y_p^+ at which the gradient is zero and the Reynolds stress is a maximum increases as the Reynolds number is increased. The corresponding profiles for the Reynolds shear stress are also shown in figure 1. Fife *et al.* (2005) have made similar observations about the Reynolds stress gradient for turbulent Couette flows and other wall-bounded flows. The effect of the constant streamwise forcing proposed here counteracts the influence of the gradient of the Reynolds shear stress.

One context in which a similar feature has been observed is in the simulation of a turbulent channel flow seeded with microbubbles (Xu, Maxey & Karniadakis 2002; Maxey *et al.* 2003). Here the bubbles displace the liquid and one of the dynamic effects is to reduce the local inertia of the flow. This may be represented by a body force density acting on the flow that is proportional to the local concentration of the bubbles and the local acceleration of the fluid. On average, the streamwise component of the force opposes the flow close to the wall and accelerates the flow further away from the wall. Figure 2 shows sample profiles for the averaged streamwise component of this effective force density under various flow conditions. The orientation of the force near the wall is linked to that of the Reynolds stress gradient. For a flow seeded with denser solid particles, the force density is positive close to the wall. It is observed too that the bubbles reduce the effectiveness of momentum transfer by the Reynolds shear stress and there is a reduction in the skin friction, while for denser particles there is an increase in skin friction. While the dynamics of drag reduction by microbubbles is complex and involves many factors, the results provide a motivation for the present study and suggest that the effect of streamwise forcing is worth investigating as an independent issue.

As we will show, the imposition of a streamwise forcing substantially modifies both the mean flow and the turbulence in the near-wall region. In the following sections, we summarize the simulation procedures and then give results for the change in skin friction as the parameters of the forcing are varied. Following this, the influence of the forcing on turbulence structure is discussed, considering both the effects of strong forcing and intermediate levels.

Group	Re_τ	Re_0	L_1/h	L_3/h	N_1	N_2	N_3	$-\mathrm{d}P/\mathrm{d}x_1$
AA	135	3000	2π	2π	64	1×65	64	0.002018
AB	135	3000	2π	2π	96	5×21	96	0.002018
B	192	4500	2π	2π	128	4×37	128	0.001805
C	380	10 000	2π	π	256	8×31	256	0.001455
D	633	18 000	2π	π	384	10×37	384	0.001234

TABLE 1. Simulation parameters: Reynolds numbers; domain size; numerical resolution including the number of elements and the spectral order; and mean pressure gradient, scaled by $\rho U_0^2/h$, of the base flow.

2. Near-wall forcing and simulation method

Simulations of turbulent Poiseuille flow in a channel are performed by numerical integration of the momentum equations for incompressible flow

$$\frac{\partial \tilde{\boldsymbol{u}}}{\partial t} + \tilde{\boldsymbol{u}} \cdot \nabla \tilde{\boldsymbol{u}} = -\frac{1}{\rho} \nabla \tilde{p} + \nu \nabla^2 \tilde{\boldsymbol{u}} + \frac{1}{\rho} \boldsymbol{F}, \qquad (2.1)$$

where ρ is the fluid density and γ is the kinematic viscosity. In the channel, the fluid velocity $\tilde{\boldsymbol{u}}(\boldsymbol{x}, t)$ is determined for $0 < x_1 < L_1$ and $0 < x_3 < L_3$ with the rigid planar walls located at $x_2 = \pm h$. No-slip boundary conditions are applied at the walls with periodic boundary conditions in both the streamwise, x_1, and spanwise, x_3, directions. The fluid velocity $\tilde{\boldsymbol{u}}$ may be written as the sum of a mean $\boldsymbol{U}$ and a fluctuating $\boldsymbol{u}$ component. In these simulations, variables are scaled by h and a fluid velocity scale U_0, with the fluid density $\rho = 1$. Under conditions of laminar flow, U_0 is the centreline velocity for the corresponding parabolic velocity profile and the value of $Re_0 = U_0 h/\nu$ specifies the kinematic viscosity. In the simulations, a constant flow rate is set and the bulk velocity U_B is maintained at a constant value of $2U_0/3$ by a control procedure that adjusts the mean pressure gradient $-\mathrm{d}P/\mathrm{d}x_1$. This ensures that the Reynolds number $Re_B = U_B h/\nu$ is fixed for any simulation.

Equation (2.1) is solved in terms of primitive variables using a spectral/hp element scheme (Karniadakis & Sherwin 2005). Fourier pseudospectral representations are used in the two periodic directions together with de-aliasing procedures for the nonlinear terms. Spectral elements are chosen in the wall-normal direction to ensure good resolution in both the near-wall regions and in the core of the channel. A third-order stiffly stable scheme, based on an explicit backwards differencing, is used for the integration in time. Details of the scheme are given in Karniadakis & Sherwin (2005, see pp. 426–430). Table 1 summarizes the different simulation conditions, listing the domain size and numerical resolution, including the number of spectral elements used at each Reynolds numbers. The Reynolds number $Re_\tau = u_\tau h/\nu$, based on the friction velocity u_τ, is varied between 135 and 633. Further details of the simulations are given by Xu (2005).

The results for the turbulence statistics of the base flows, without any streamwise forcing, are in good agreement with results such as Moser, Kim & Mansour (1999) for channels of comparable length L_1. Del Álamo & Jiménez (2003) and del Álamo et al. (2004) have demonstrated that longer channels are required to fully resolve some of the large-scale turbulent features that span both the core of the channel and the near-wall region. However, for the purposes of the present parametric study of the effects of streamwise forcing, the choice of $L_1/h = 2\pi$ is adequate to provide
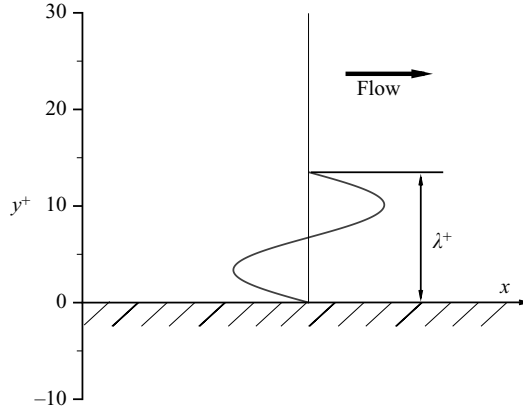
FIGURE 3. Idealization of the excitation force and notation; see equation (2.2).

self-consistent results at a reasonable computational cost. Jiménez, del Álamo & Flores (2004) have shown that these larger-scale structures do not significantly contribute to the Reynolds shear stress near the wall.

The streamwise forcing is specified by the force density $\boldsymbol{F}(x_2) = (F_1, 0, 0)$ and has the form shown in figure 3. In particular, the force density is given by

$$\left.\begin{aligned} F_1(y) &= -\rho I \sin\left(\frac{2\pi}{\lambda}y\right) \quad (0 \leqslant y \leqslant \lambda), \\ F_1(y) &= 0 \qquad\qquad\qquad (y > \lambda), \end{aligned}\right\} \tag{2.2}$$

where $y = h \pm x_2$ is the distance from the nearest planar boundary. (Throughout the paper, y is used to denote distance from the wall.) This forcing acts to decelerate the flow close to the wall, $0 < y < \lambda/2$, and then accelerate the flow in the adjacent region $\lambda/2 < y < \lambda$. Overall the total force, integrated across the channel, is zero and the mean pressure gradient balances the skin friction to within the limits of numerical resolution. We parameterize the force density with two parameters I and λ, representing the amplitude and the spatial region of the excitation, respectively. The amplitude of the force density I may be scaled in convective flow variables by U_0^2/h or in terms of wall variables as $I^+ = I\nu/u_\tau^3$, using the value of u_τ for the unforced flow. Similarly, λ may be given in terms of wall variables as λ^+ or as λ/h.

3. Results on drag reduction

In figure 4, we first show representative results at $Re_\tau = 135$ for the effect of varying λ^+ on the turbulent drag over time. The drag is normalized by the mean drag of the base flow without forcing. The value of the forcing amplitude is kept constant at $I = 0.02$ (in convective units), $I^+ = 0.073$. We see that for the two lower values of λ^+ a persistent, long-term drag reduction is achieved, whereas for the largest value of $\lambda^+ = 35.1$ there is only a transient drag reduction. Later, this transient reduction gives way to either no drag reduction or a small increase in drag. A similar transient reduction in drag, followed by a drag increase was found for $\lambda^+ = 59.4$, while for $\lambda^+ = 27$ there was a sustained reduction in drag of about 14%.

If the length scale of the forcing is fixed at $\lambda^+ = 18.9$ and the amplitude I is varied, then sustained drag reduction is also achieved (figure 5). The level of drag reduction
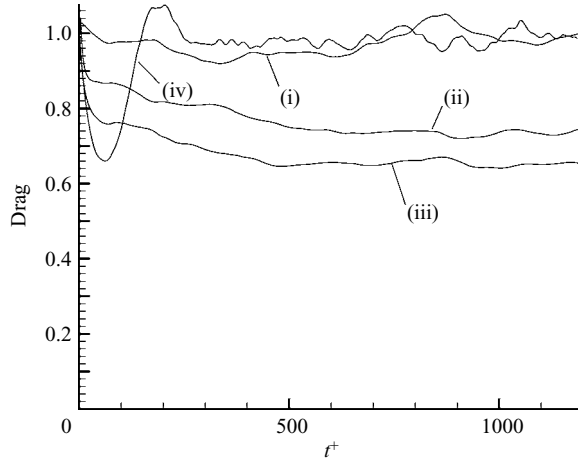
FIGURE 4. Time history of the normalized skin friction at $Re_\tau = 135$, with $I^+ = 0.073$ ($I = 0.02$), for: (i) No forcing; (ii) $\lambda^+ = 13.5$; (iii) $\lambda^+ = 18.9$; (iv) $\lambda^+ = 35.1$.
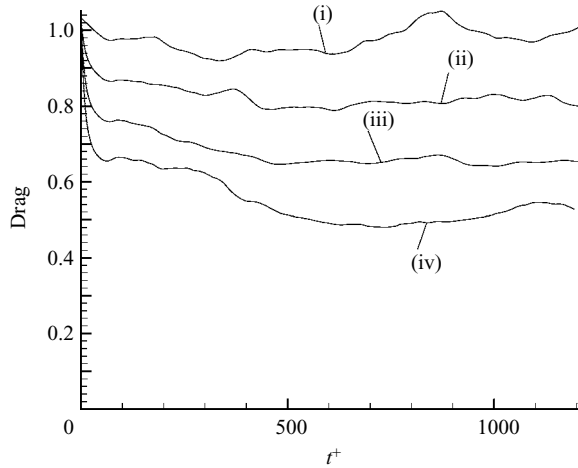

FIGURE 5. Time history of normalized skin friction for $\lambda^+ = 18.9$ and different amplitudes I at $Re_\tau = 135$: (i) No forcing; (ii) $I^+ = 0.0365$ ($I = 0.01$); (iii) $I^+ = 0.073$ ($I = 0.02$); (iv) $I^+ = 0.109$ ($I = 0.03$).

increases as the forcing amplitude is increased, but for amplitudes larger than $I^+ = 0.1$ there was no apparent additional reduction in the long-term drag.

Results on the long-term change in drag at $Re_\tau = 135$ are given in table 2. The results were obtained by integrating the equations of motion for $t^+ = 0$–600, to allow for possible transients, and the averages were then obtained by averaging over the following time interval $t^+ = 600$–1200. Additionally, a higher resolution was used in the simulations (group AB) for $\lambda^+ = 13.5, 18.9$ to ensure that small-scale features produced by the forcing were fully resolved. The results show that for $\lambda^+ = 13.5$, a 79 % reduction in skin friction can be achieved. This is, in fact, a lower skin friction than for laminar flow. For $\lambda^+ = 27$, the maximum level of drag reduction that is achieved is substantially lower than that for the two smaller values of λ. These results indicate that there is some preferred range of values for I and λ to achieve a sustained

λ	λ^+	$I=0.01$ $I^+=0.0365$	0.015 0.0547	0.02 0.073	0.03 0.109	0.05 0.183	0.1 0.365	0.2 0.73
0.1	13.5	−18 %	−25 %	−26 %	−33 %	−53 %	−73 %	−79 %
0.14	18.9	−19 %	−26 %	−34 %	−49 %	−49 %	−47 %	
0.2	27	−10 %	−12 %	−14 %	−13 %	−6 %	−14 %	

TABLE 2. Approximate percentage change in long-term drag at $Re_\tau=135$ for various λ and I. Data from group AB except for $\lambda^+=27$ which is from group AA.

reduction in drag. The results in table 2 are ambiguous, and complicated by a direct contribution of the forcing to the reduction in skin friction. A more careful analysis is required to interpret the results.

Reduction in drag is closely linked to reductions in the mean turbulent Reynolds shear stresses. However, as pointed out by Fukagata, Iwamoto & Kasagi (2002) changes in both the peak value and the profile contribute. This is evident from taking integral moments of the equation for the mean flow (1.1). The zero-order moment, which is a simple integral across the channel, gives the usual result that in a final stationary state, the mean pressure gradient balances the effect of the combined mean shear stress from the two walls, since the applied forcing exerts no net force on the flow. The second moment yields

$$\tfrac{1}{2}[\tau(h) + \tau(-h)] = \frac{3\mu U_B}{h} - \frac{3}{2h^2}\int_{-h}^{h} x_2(-\rho\overline{u_1 u_2})\,\mathrm{d}x_2 + \frac{3}{4h^2}\int_{-h}^{h} x_2^2 F_1\,\mathrm{d}x_2, \qquad (3.1)$$

where $\tau(\pm h)$ is the mean shear stress at the respective walls. The first term on the right-hand side is equal to the corresponding drag for laminar flow for the given flow rate U_B. The contributions from the laminar drag and the mean Reynolds shear stress, when scaled by ρu_τ^2 for the base flow, are denoted by K_L and K_T, respectively.

There is also a direct contribution of the forcing F_1 in (3.1), that tends to reduce the drag. This may be calculated from (2.2) and when scaled by ρu_τ^2, is denoted by K_F. This contribution is

$$K_F = -\frac{3}{4}\frac{I\lambda}{\pi u_\tau^2}\frac{\lambda}{h}\left(2 - \frac{\lambda}{h}\right). \qquad (3.2)$$

Overall, the balance for the normalized skin friction is

$$[\tau(h) + \tau(-h)]/(2\rho u_\tau^2) = K_L + K_T + K_F. \qquad (3.3)$$

At $Re_\tau=135$, the contribution from the forcing K_F is significant. For $\lambda^+=13.5$ and $I^+=0.073$, $K_F=-0.045$ and varies linearly with the forcing amplitude so that at the largest forcing amplitude, $I^+=0.73$, $K_F=-0.45$. At this forcing amplitude, the overall reduction in the normalized drag is 79 %, of which 45 % comes from K_F and only 34 % from the reduction in the value of K_T. The effect of K_F leads to a value for the skin friction that is lower than that for laminar flow.

Figure 6 shows the variation of K_T corresponding to the results in table 2. At this Reynolds number, $K_T=0.667$ and $K_L=0.333$ in the absence of any forcing. For $\lambda^+=13.5$, there is a substantial reduction in the Reynolds stress component K_T with a clear minimum evident around $I^+=0.365$. For $\lambda^+=18.9$, the minimum for K_T occurs around $I^+=0.109$, but is less pronounced. The initial decrease of K_T though is somewhat faster than for $\lambda^+=13.5$. This and the more significant contribution from K_F accounts for the comparable levels of drag reduction at these two length scales.
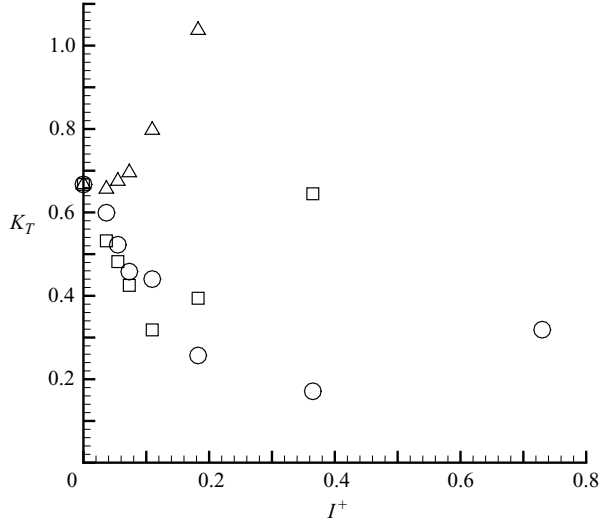
FIGURE 6. Reynolds stress contribution K_T to skin friction at $Re_\tau = 135$ for $\lambda^+ = 13.5$ (circles), $\lambda^+ = 18.9$ (squares) and $\lambda^+ = 27$ (triangles) for different amplitudes I^+.
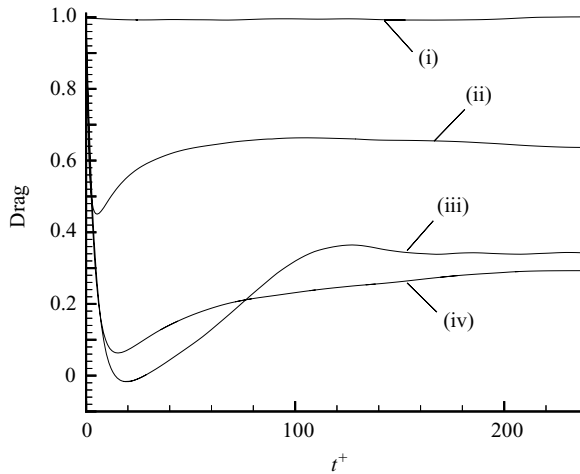

FIGURE 7. Time history of the normalized skin friction at $Re_\tau = 633$ with $I^+ = 0.513$ ($I = 0.4$): (i) no forcing; (ii) $\lambda^+ = 7.0$; (iii) $\lambda^+ = 13.3$; (iv) $\lambda^+ = 12.0$.

For $\lambda^+ = 27$, there is a minimal decrease K_T at the lowest forcing amplitude, but otherwise K_T increases rapidly for larger amplitudes. The modest levels of reduction in skin friction shown in table 2 for $\lambda^+ = 27$ are due to K_F. There are competing effects from K_T, which tends to increase the skin friction, and K_F, which scales linearly with amplitude, tends to reduce the skin friction. These results overall show that for the forcing to be effective in reducing turbulent contributions to the skin friction, the length scale λ^+ should be 20–25 or less.

At $Re_\tau = 633$, the general features are the same but the level of sustained reduction in the turbulent drag is more significant. Figure 7 shows the initial time history of the normalized skin friction. For $\lambda^+ = 12.0$, there is a transient period with up

Index	Re_τ	I	I^+	λ	λ^+	$I\lambda/\pi u_\tau^2$	Re_S	$\Delta Drag$
A1	135	0.02	0.073	0.1	13.5	0.31	28	-26%
A2	135	0.03	0.109	0.1	13.5	0.47	43	-33%
A3	135	0.1	0.365	0.1	13.5	1.57	143	-73%
B1	192	0.04	0.116	0.064	12.3	0.45	34	-19%
B2	192	0.06	0.174	0.064	12.3	0.68	51	-30%
B3	192	0.08	0.232	0.064	12.3	0.91	69	-39%
C1	380	0.1	0.18	0.034	12.9	0.74	62	-34%
C2	380	0.15	0.27	0.034	12.9	1.11	92	-47%
C3	380	0.2	0.36	0.023	8.7	1.00	38	-33%
C4	380	0.2	0.36	0.034	12.9	1.48	123	-70%
C5	380	0.2	0.36	0.036	13.7	1.57	147	-63%
C6	380	0.2	0.36	0.04	15.2	1.74	201	-52%
C7	380	0.2	0.36	0.05	19	2.18	393	-35%
D1	633	0.4	0.513	0.011	7.0	1.14	28	-35%
D2	633	0.4	0.513	0.017	10.8	1.76	103	-68%
D3	633	0.4	0.513	0.019	12.0	1.96	141	-71%
D4	633	0.4	0.513	0.021	13.3	2.17	192	-65%

TABLE 3. Approximate long-term percentage reduction in turbulent drag from simulations at $Re_\tau = 135, 192, 380, 633$, for various values of I and λ. Re_S is defined in (4.2).

to 90 % drag reduction followed by sustained drag reduction of 70 %, whereas for $\lambda^+ = 13.3$ there is a larger transient, but a slightly lower level of the final sustained drag reduction for the same level of the force amplitude. At this Reynolds number, $K_L = 0.090$ while $K_F = -0.055$ for the results shown at $\lambda^+ = 12$. The contribution K_T of the Reynolds shear stress to the skin friction balance (3.3) is now more significant and the reductions in drag directly reflect the reductions in K_T.

The evolution of the normalized drag following the start of the forcing shown in figure 7 and in figures 4 and 5 is given in terms of t^+. The time scale for the transient adjustment period at $Re_\tau = 633$ is about $t^+ = 0$–200 and thereafter is in equilibrium. At $Re_\tau = 135$, there is a similar transient interval, measured in terms of t^+ in figure 4, although there is a longer-term fluctuation in the skin friction even for the base flow.

A summary of results for a range of Reynolds numbers is given in table 3, covering $Re_\tau = 135$–633 for selected values of the forcing parameters. Reductions in the turbulent drag on the channel walls of approximately 70 % may be achieved throughout this range. As the Reynolds number is increased, the direct contribution of the forcing to the drag balance (3.3) K_F, given by (3.2) becomes less important. The optimal value of λ^+ is consistently in the range $\lambda^+ = 12$–14, even as the Reynolds number is varied. The negative counter-stream portion of the streamwise force density then acts within the region $y^+ < 7$. This corresponds to the region in which the Reynolds stress gradient of the base flow, shown in figure 1, is positive and increasing towards its maximum value.

The forcing amplitude I and the Reynolds stress gradient term $\partial\overline{u_1 u_2}/\partial y$ have the same dimensions and may be compared. In terms of wall variables, the maximum Reynolds stress gradient shown in figure 1 is less than 0.07. The typical value of I^+ required for drag reduction, as given in table 3, is substantially larger. At $Re_\tau = 135$, for case A1, $I^+ = 0.073$ yet a larger value of $I^+ = 0.365$ is required for the stronger drag reduction in case A3. At higher Re_τ, the values of I^+ are larger also. The integrated
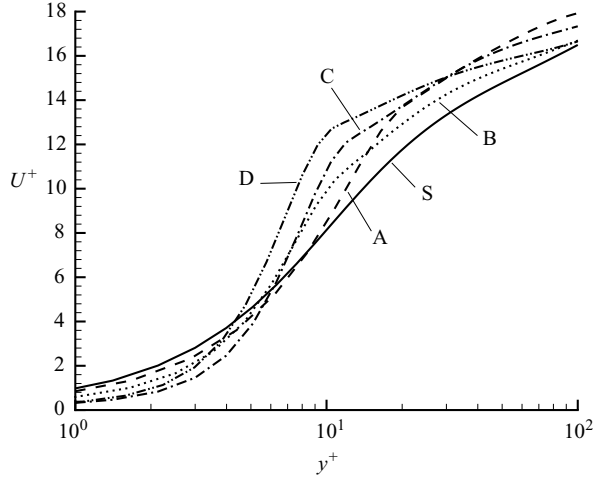
FIGURE 8. Mean velocity profiles U^+, normalized with u_τ of the base flow: (A) case A1; (B) case B3; (C) case C4; (D) case D3. The solid line (S) represents the no-control case at $Re_\tau = 380$.

negative contribution of the force density (2.2) retarding the near-wall flow is

$$\int_0^{\lambda/2} F_1(y)\,\mathrm{d}y = -\rho I \lambda/\pi. \tag{3.4}$$

Dimensionally, $I\lambda/\pi$ scales with u_τ^2, or in terms of wall variables equals $I^+\lambda^+/\pi$, and may be compared with the wall shear stress of the base flow. At $Re_\tau = 135$, for case A3 this gives a corresponding value of $I^+\lambda^+/\pi$ equal to 1.57. The preferred combinations of I and λ at other Reynolds numbers give values of $I^+\lambda^+/\pi$ in the range $1 < I^+\lambda^+/\pi < 2$ (table 3). In order to achieve the higher levels of drag reduction, the magnitude of the retarding force required is thus comparable to the wall shear stress of the base flow.

4. Flow modification

In this section, we consider the way in which the flow is modified by the streamwise forcing, and specifically the factors limiting the higher levels of drag reduction and some of the characteristics at lower forcing levels.

4.1. *Mean velocity profile*

The first consideration is the change in the mean flow and especially how this changes in the near-wall region. Figure 8 shows the mean flow at several different Reynolds numbers with the forcing applied. These profiles are compared to the mean velocity of the base flow at $Re_\tau = 380$, without forcing, and the mean velocity is scaled by u_τ, corresponding to the flow with no forcing. For all the forced flows, the mean velocity is markedly different from the standard profile. The gradient at the wall is reduced, but the slope increases sharply away from the wall, consistent with the formation of an inflection in the mean velocity profile. For case A1, based on $\lambda^+ = 13.5$ and $I^+ = 0.073$ at $Re_\tau = 135$, the reduction in drag is 21 % and the change in the mean velocity is less steep than for the other cases, whereas at $Re_\tau = 633$ (case D3) the reduction in drag is 70 %.
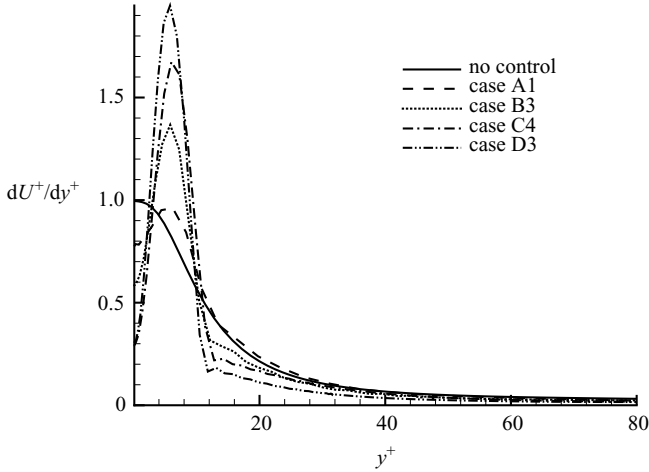
FIGURE 9. Profiles of normalized mean velocity gradient in wall variables for cases A1, B3, C4 and D3. Values of $\lambda^+ = 12$–13.5. The solid line is the no-control result at $Re_\tau = 380$.

More revealing are the profiles for the mean velocity gradient (figure 9). In all the forced flows shown, $\lambda^+ = 12$–13.5 and correspond to significant levels of reduction in skin friction. The formation of a strong shear layer centred at $y^+ = 6$–7 is clearly evident, with reduced mean shear both at the wall and beyond the shear layer, $y^+ > 12$. The peak value of the mean velocity gradient, given in terms of wall variables, increases with higher levels of drag reduction and corresponding increases in Reynolds number and forcing amplitude. If the turbulence is indeed strongly suppressed and there is a purely laminar viscous response to the near-wall forcing in (1.1), then the result would be a local additional component to the mean shear

$$\frac{\partial U_1}{\partial x_2} = \frac{I\lambda}{2\pi\nu} \left\{ 1 - \cos\left(\frac{2\pi y}{\lambda}\right) \right\} \tag{4.1}$$

for $0 \leqslant y \leqslant \lambda$, and zero otherwise. Here, as in (2.2), y denotes distance from the wall. This has a maximum at $y^+ = \lambda^+/2$, with a peak additional mean shear of $I^+\lambda^+/\pi$ when scaled by wall variables. Referring back to the prior discussion of the forcing levels, we can see that the observed peak value of $(\partial U_1/\partial x_2)^+$ at $Re_\tau = 633$ is close to the value of $I^+\lambda^+/\pi = 1.96$ for this case (D3). Other factors contributing to this near-wall maximum of the mean velocity gradient are the mean shear in response to the pressure-driven flow, which tends to increase the peak value, whereas any Reynolds shear stresses would tend to decrease the peak value.

4.2. Reynolds stresses

Profiles of the r.m.s. velocity fluctuations at $Re_\tau = 380$ for cases C2 and C4 are compared in figure 10 with the results for the unforced flow. In both cases, $\lambda^+ = 12.9$. All three peak values of u_1', u_2' and u_3' are reduced. For the stronger forcing of case C4 ($I^+ = 0.36$) the reduction is at least 40%. For other cases at lower Reynolds numbers, where the level of drag reduction is less, the reduction of the r.m.s. fluctuations is smaller.

Figure 11 shows Reynolds stress profiles at $Re_\tau = 135$ and 380. At the lowest simulated Reynolds number, $Re_\tau = 135$, there are significant reductions in the Reynolds shear stress, which are stronger as the forcing amplitude is increased. As shown in (3.1), the change in wall drag depends on the integral moment K_T of the Reynolds
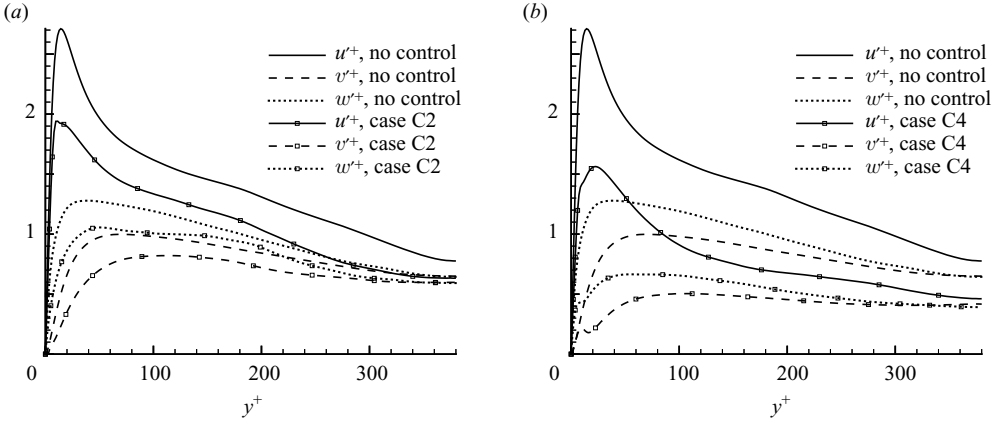
FIGURE 10. Profiles of r.m.s. velocity fluctuations at $Re_\tau = 380$, scaled by u_τ for the no-control flow, comparing no-control results to results for (a) case C2 and (b) case C4: u'_1, solid line; u'_2, dashed line; u'_3, dotted line. Lines with symbols denote forced flow results.
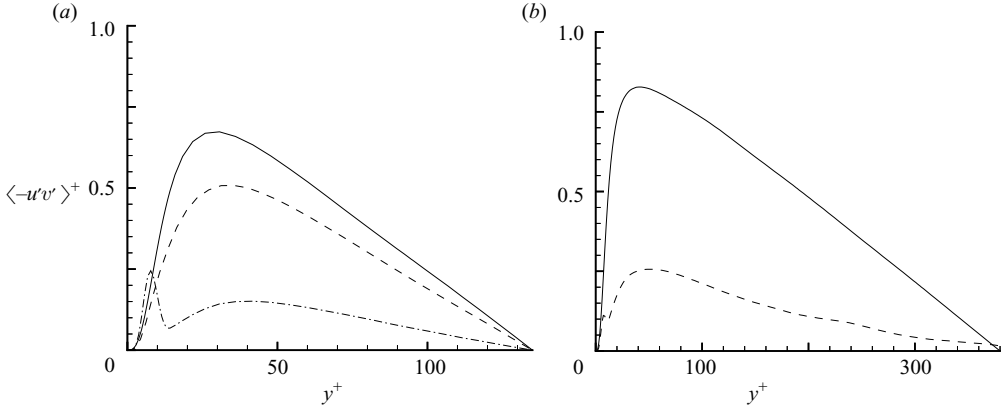

FIGURE 11. Profiles of Reynolds shear stress: (a) $Re_\tau = 135$, for cases A1 (dashed line) and A3 (dashed-dotted line); (b) $Re_\tau = 380$ for case C4. Solid lines denote the no-control results.

shear stress. Both a reduced peak value or a shift of the peak away from the wall will act to reduce K_T. We see that for case C4, at $Re_\tau = 380$, the peak value is reduced by 70 % and the location of the peak is shifted away from the wall. There is also a shift in the peak Reynolds stress for case C2 (not shown), where $I^+ = 0.27$. At the lower forcing level, case C2, there is still a strong mean shear layer with a maximum mean shear $(\partial U_1/\partial x_2)^+ = 1.4$.

Close to the wall, there is a significant variation in the Reynolds shear stress that is sensitive to the value of the length scale λ of the streamwise forcing. Figure 12 shows the near-wall profiles at $Re_\tau = 380$ for several values of λ^+ with a fixed value of $I^+ = 0.36$. For case C4, where $\lambda^+ = 12.9$, the Reynolds stress is substantially reduced throughout the flow with a small local maximum at around $y^+ = 8$. If $\lambda^+ = 8.7$ (case C3), the drag reduction is much less, only 30 %, and the change in Reynolds stress is smaller. For the somewhat larger value of $\lambda^+ = 13.7$ (case C5), there is a strong near-wall local maximum even though the Reynolds stress is reduced elsewhere. The reduction in drag is also slightly less here, 67 % as opposed to 70 %.
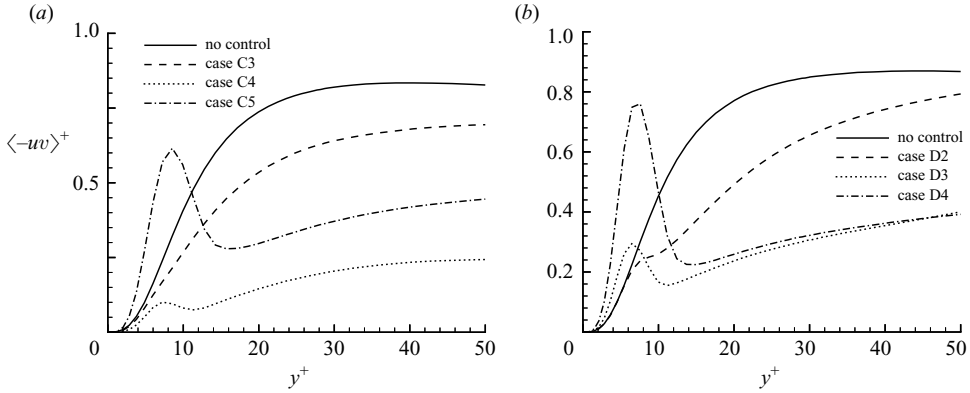
FIGURE 12. Near-wall profiles of Reynolds stress at (*a*) $Re_\tau = 380$ for cases: C3, dashed line; C4, dotted line; C5, dashed-dotted line; and (*b*) at $Re_\tau = 633$ for cases: D2, dashed line; D3, dotted line; D4, dashed-dotted line.

The same general features are repeated in figure 12 for $Re_\tau = 633$ with a fixed forcing amplitude $I^+ = 0.513$. Again the largest drag reduction, case D3 with $\lambda^+ = 12$, is associated with a greatly reduced overall Reynolds shear stress. There is a small local maximum in the Reynolds stress near the wall. For the slightly larger length scale $\lambda^+ = 13.3$, case D4, the near-wall maximum is much stronger and occurs at approximately $y^+ = 7.5$, within the shear layer.

This local increase in the near-wall Reynolds stress is linked to the formation of the shear layer by the near-wall forcing. On the assumption of strong near-wall forcing, we may estimate a local Reynolds number Re_S for the shear layer using the estimated mean shear given by (4.1). Re_S is defined in terms of the level of mean shear and the length scale λ as

$$Re_S = \frac{I\lambda^3}{2\pi\nu^2}. \tag{4.2}$$

There is a strong cubic dependence of Re_S on the value of λ. Values of Re_S for the different cases that have been computed are given in table 3. For case D3, $Re_S = 141$ and a small peak forms in the Reynolds stress forms whereas for case D4, $Re_S = 192$ and there is a strong local peak. Values of Re_S in the range of $Re_S = 120$–140 correlate with changes in the near-wall response to the forcing and the formation of a local near-wall peak in the Reynolds shear stress at other Reynolds numbers. At $Re_\tau = 380$, the case C4 gives $Re_S = 123$, where only a small peak forms, whereas for the clear near-wall peak of case C5, $Re_S = 147$.

At $Re_\tau = 135$ there is a similar response and for case A3, where $Re_S = 143$, a near-wall peak forms in the Reynolds stress (figure 11), comparable to that of case D3 (figure 12). The values of K_T for the integral moment of the Reynolds stress shown in figure 6 also follow the same pattern. K_T takes its lowest value for case A3 when $\lambda^+ = 13.5$, and for $\lambda^+ = 18.9$, the lowest value of K_T shown corresponds to $Re_S = 117$ at $I^+ = 0.109$. The next data point corresponds to $Re_S = 195$. Similarly, for $\lambda^+ = 27$, at the lowest level of forcing $I^+ = 0.0365$, $Re_S = 114$ and there is a small reduction in K_T. For the other values of I^+ shown, $Re_S > 170$.

The level of drag reduction and reduction of the turbulent velocity fluctuations is limited then by the value of Re_S. Forcing at amplitudes I or length scales λ where Re_S exceeds 140 yields no further reductions and sets an upper limit. Taken together with

the discussion at the end of the previous section, these conditions set a working range for I and λ for which reductions in the turbulence may be expected. The sensitivity of Re_S to changes in λ means that even small changes can result in Re_S exceeding the threshold. The level of drag reduction does not necessarily change dramatically as is evident by comparing cases C4 and C5 or D3 and D4. The increase in Reynolds stress that occurs initially for $Re_S > 140$ is confined locally to a region near the wall and extends about 15 wall units or less. The overall change in the Reynolds stress moment K_T is relatively small and so too is the change in skin friction (3.3).

4.3. *Vorticity fluctuations and instantaneous flow features*

The r.m.s. vorticity fluctuations also exhibit significant near-wall variations when the streamwise forcing is applied. Figure 13 shows profiles of the vorticity fluctuations of both the base flow and the forced flows, cases C4 and C5, at $Re_\tau = 380$. At the wall, the spanwise component ω'_3 has the largest fluctuation levels, which are associated with the fluctuations in the streamwise component of the wall-shear stress. This is substantially reduced for case C4 as is ω'_1 and the wall-normal component ω'_2, where the latter goes to zero at the wall because of the no-slip flow condition. With the forcing there is a simple, local maximum of ω'_2 at around $y^+ = 8$, closer to the wall than in the unforced flow. There is also a more pronounced local maximum in ω'_1 at around $y^+ = 8$. The case C5, where λ is slightly larger, has significantly increased vorticity fluctuations near the wall, while the fluctuations are all reduced for $y^+ > 20$.

These results at $Re_S = 123$ and $Re_S = 147$, respectively, for cases C4 and C5 may be compared with those at a lower forcing amplitude, case C2, where $Re_S = 92$. The three components of the r.m.s. vorticity fluctuations are shown in figure 14 and may be compared with those in figure 13. All three components are significantly lower than for the base flow and do not exhibit any near-wall peaks. The spanwise vorticity fluctuations ω'_3 are reduced overall, but are relatively stronger for $y^+ < 10$.

The changes in the turbulence due to the near-wall forcing are more evident from a visualization of the instantaneous flow vorticity. This is done using the second invariant Q for the velocity gradient, $Q = (\partial \tilde{u}_i / \partial x_j)(\partial \tilde{u}_j / \partial x_i)$. A contour plot of the regions where $Q^+ < -0.0142$ highlights the dominant vorticity structures in the flow. The near-wall vortices are shown in figure 15 for a portion of the flow domain, comparing the base flow with the forced flow C4 at $Re_\tau = 380$. The formation of vortex loops lifting away from the wall is completely suppressed with the forcing applied. Instead, there are regularly spaced spanwise structures within the region $y^+ < 20$. The standard turbulent processes near the wall are replaced by those characteristic of a shear layer in transition. When λ^+ is increased to 13.7, case C5, then the shear layer begins to create its own three-dimensional turbulence structures. The corresponding contour plot of Q^+ for case C5 (see figure 16) shows increased turbulence, but the vorticity-dominated features are still confined to the near-wall region, $y^+ < 50$.

These features are again consistent with the formation of a local shear layer centred just above the wall at $y^+ \sim 6$–7, driven by the streamwise forcing. It would appear that case C4 corresponds to a near-optimal condition of marginal stability for the local shear layer. The increase in Re_S from 123 to 147 in case C5 leads to a transition in the shear layer and the turbulence. The suppression of three-dimensional vortex structures is less evident at lower forcing levels. Examination of a contour plot of Q^+ for case C2 shows no obvious special features.

We examine the formation of low-speed streaks in the near-wall zone in figure 17, where the contours for the instantaneous streamwise velocity for case C4 are compared to those of the base flow. At $y^+ = 5$, there is a predominance of low-speed (u_1) fluid
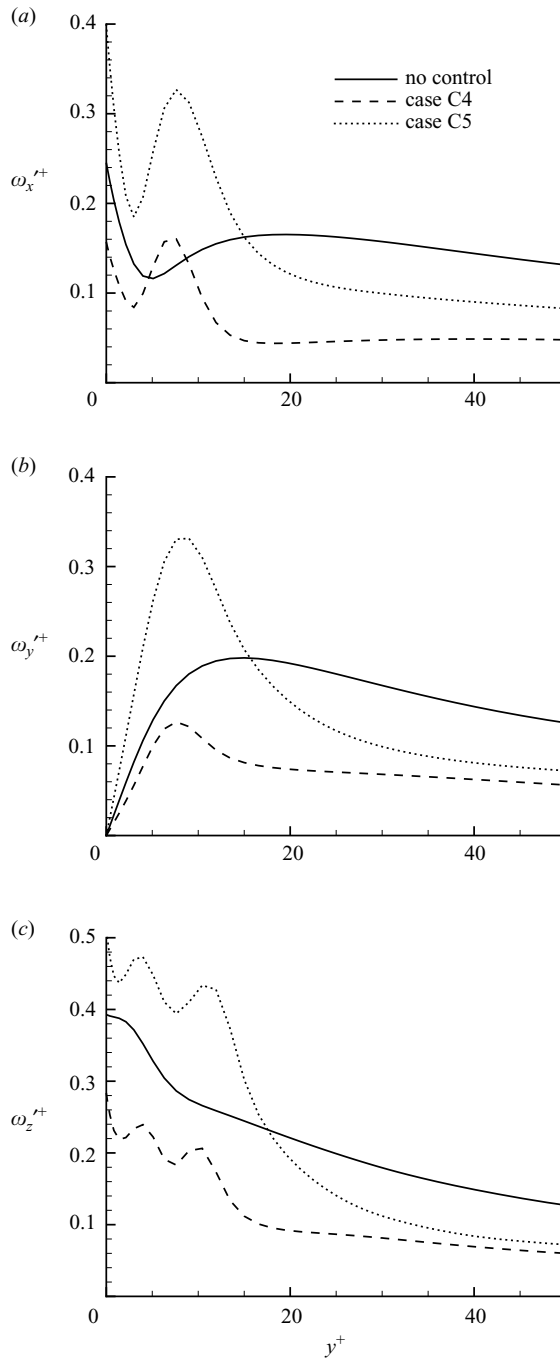
(a)

(b)

(c)

FIGURE 13. Profiles of r.m.s. vorticity fluctuations at $Re_\tau = 380$: (a) $\omega_1'^+$; (b) $\omega_2'^+$; (c) $\omega_3'^+$. Results for $\lambda^+ = 12.9$, case C4; $\lambda^+ = 13.7$, case C5; no-control.

for the forced flow with elongation of the low-speed streaks. At $y^+ = 10$, there is now an absence of low-speed fluid in the forced flow while the individual regions of moderate- or faster-speed fluid are both longer and wider. Even at $y^+ = 30$, outside
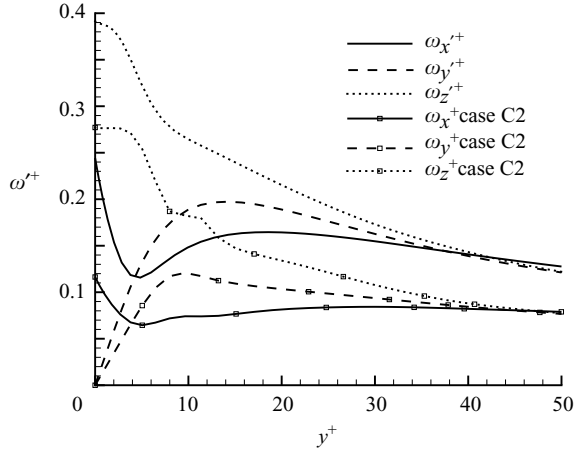
FIGURE 14. Profiles of r.m.s. vorticity fluctuations at $Re_\tau = 380$ for case C2.
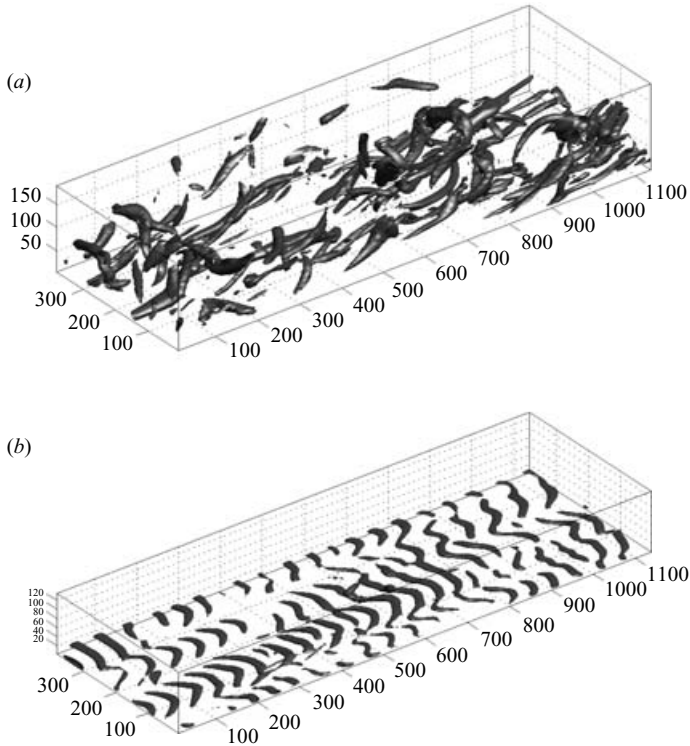
FIGURE 15. Contours of Q at $Re_\tau = 380$, (a) no control and (b) case C4. The region shown is $0 < x_1^+ < 1190$, $0 < x_3^+ < 380$.

of the shear layer and the spanwise structures seen in figure 15, there is again an absence of low-speed fluid in the forced flow. This indicates that the usual processes of exchange of high- and low-speed fluid between the near-wall region and the buffer layer are greatly reduced by the presence of the shear layer.
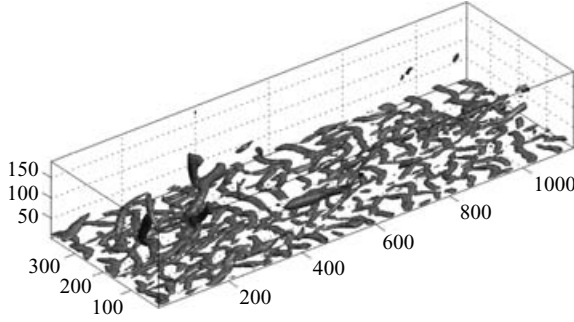
FIGURE 16. Contours of Q at $Re_\tau = 380$ for case C5.

Figure 18 shows the instantaneous velocity fluctuations for u_1 and u_2 arranged as a quadrant plot at $y^+ = 13.5$ for the base flow and case A2 at $Re_\tau = 135$. This plane corresponds to the outer edge of the forcing. The fluctuations are scaled by u_τ of the base flow. As usual, there are strong contributions to the Reynolds shear stress from both the second and fourth quadrants. The streamwise velocity flucuations are comparable between the two cases; however, the u_2 fluctuations are significantly lower for the forced flow and show no large deviations. The reduction in the friction velocity for case A2 is only 18 % and the changes in u_2 are more significant than this.

At the higher Reynolds number of $Re_\tau = 380$, figure 19 shows a similar quadrant plot of the instantaneous velocity u_1, u_2 fluctuations for cases C1 and C4 at $y^+ = 11.3$. For both cases, $\lambda^+ = 12.9$ and the plane is just within the region of flow forcing. There are significant changes as I increases by a factor of two between the two cases shown. The fluctuations for C1 are not that different from those of the base flow, while for C4 there is both a reduction in u_2 fluctuations and a change in the relative contributions of the quadrants to the Reynolds stress.

4.4. *Velocity–vorticity correlations*

When the amplitude I of the forcing is strong and the shear layer is clearly evident, it is not difficult to see the changes in turbulence structure. At lower levels of I, there may still be substantial reduction of the skin friction and changes in the turbulence correlations. These may be more evident by considering the gradient of the mean Reynolds shear stress rather than the Reynolds stress alone.

Changes to the gradient of the Reynolds shear stress can be linked to vorticity flux terms. In general, the Reynolds stress gradient is

$$\frac{\partial (\overline{u_i u_j})}{\partial x_j} = -\epsilon_{ijk} \overline{u_j \omega_k} + \frac{1}{2} \frac{\partial (\overline{u_j u_j})}{\partial x_i}. \tag{4.3}$$

As the channel flow is homogeneous in the streamwise and spanwise directions and by selecting $i = 1$, we obtain

$$\frac{\partial (\overline{u_1 u_2})}{\partial x_2} = -\overline{u_2 \omega_3} + \overline{u_3 \omega_2}, \tag{4.4}$$

where the terms $\overline{u_2 \omega_3}$ and $\overline{u_3 \omega_2}$ represent the vortex-transport and vortex-stretching contributions, respectively. Profiles for the three terms in (4.4) are shown in figure 20, comparing the results for cases C4 and C2 with that of the base flow. As the amplitude I is increased, the peak of the Reynolds stress gradient is reduced and shifted towards the wall. The vortex stretching term $\overline{u_3 \omega_2}$ is also reduced and the minimum again shifted towards the wall. For both, the most significant variations are confined to
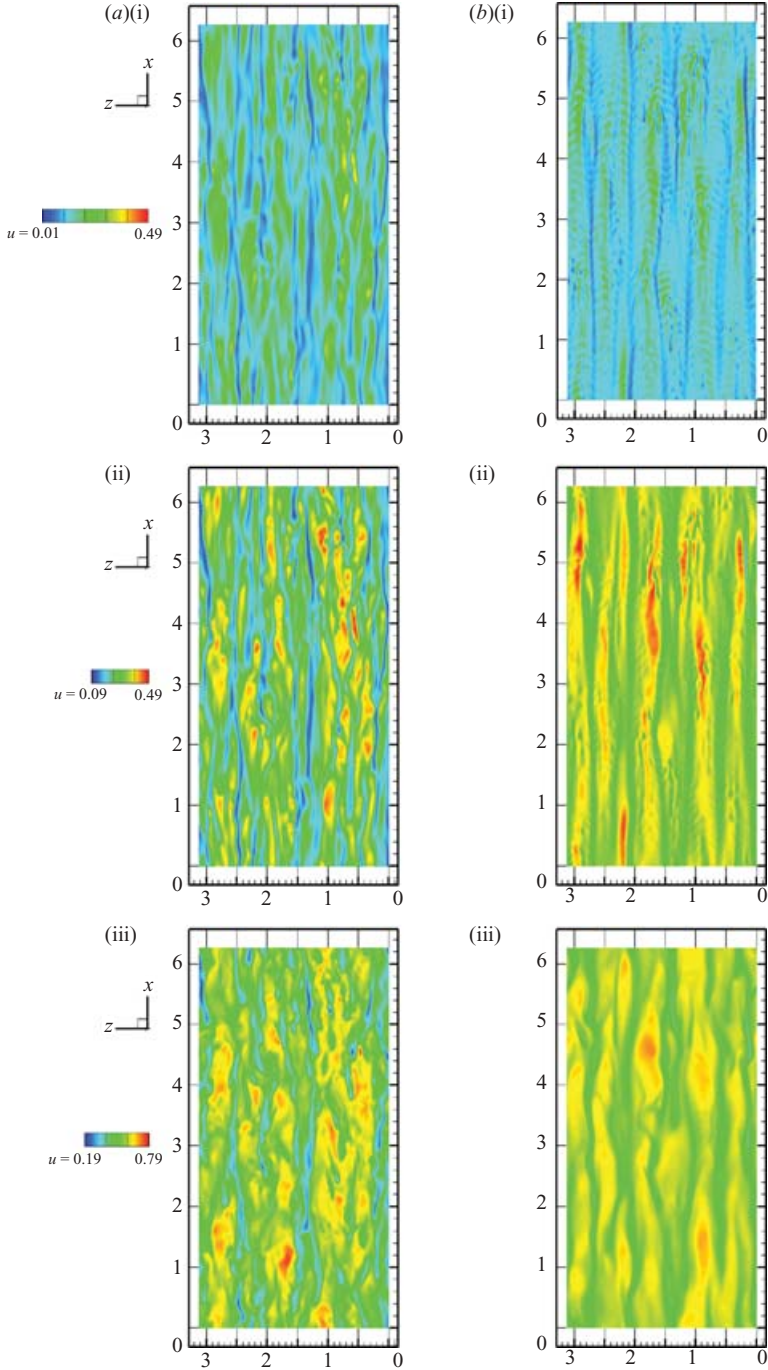
FIGURE 17. Contours of streamwise velocity in the (x_1, x_3)-plane at $Re_\tau = 380$, (a) no control and (b) case C4: (i) $y^+ = 5$; (ii) $y^+ = 10$; (iii) $y^+ = 30$.

$y^+ < 30$. The vorticity transport term $\overline{u_2\omega_3}$ is the wall-normal flux of spanwise vorticity flucutations, which in the base flow extends over a wider range. Within the forced shear layer, $y^+ < 13$, this is not significantly altered. However the vortex transport is
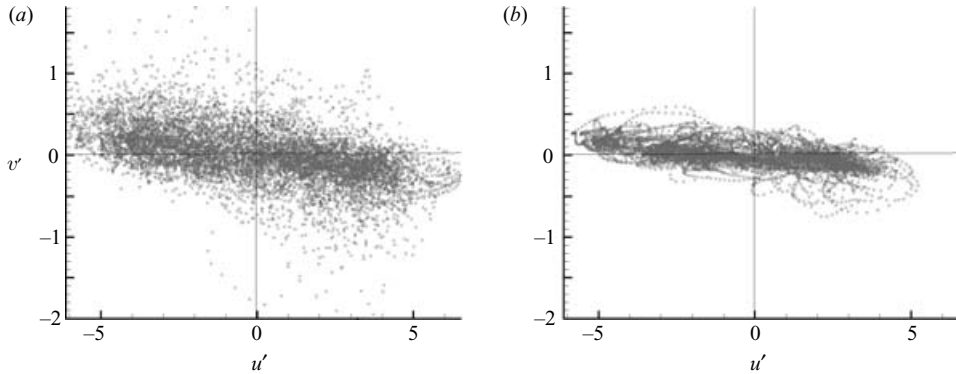
FIGURE 18. Quadrant plot for Reynolds shear stress for $Re_\tau = 135$, (*a*) base flow; (*b*) case A2, at $y^+ = 13.5$.
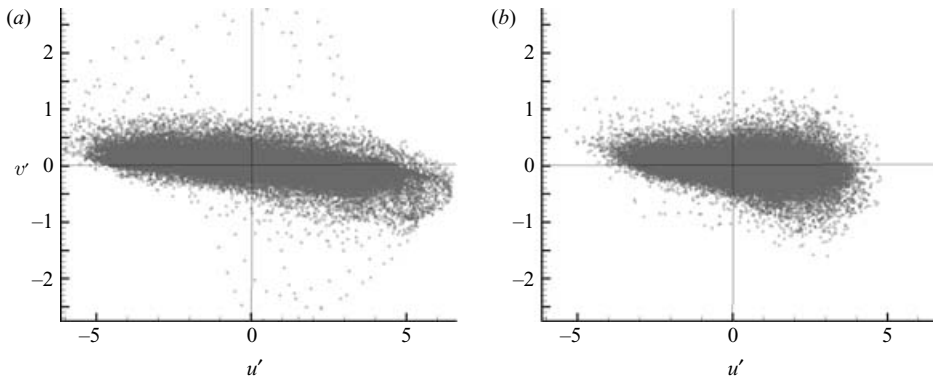

FIGURE 19. Quadrant plot for Reynolds shear stress for $Re_\tau = 380$, (*a*) case C1; (*b*) case C4, at $y^+ = 11.3$.

reduced significantly in the buffer layer and beyond, consistent with a reduction of turbulent transport outside the shear layer.

The vortex-transport term $\overline{u_2 \omega_3}$ has been identified by Jiménez & Pinelli (1999) as an important part of the autonomous cycle of near-wall turbulence in a channel flow at low to moderate Reynolds numbers. They separately filtered and reduced the vortex-transport and vortex-stretching terms to determine how this would modify the generation of near-wall streaks. They found that reducing the vortex-transport term significantly reduced the streaks and the skin friction, whereas filtering the vortex-stretching term $\overline{u_3 \omega_2}$ had little effect. Our results point to other factors also being involved.

5. Summary and discussion

We have presented an alternative technique for turbulent drag reduction, providing an overview of the main observed features. The streamwise forcing leads to the formation of a strong mean shear layer near each wall and reduces the mean velocity gradient at the wall while shifting the maximum mean shear to $y^+ = \lambda^+/2$. For larger forcing amplitudes, a maximum drag reduction of 70 % is observed with a very large reduction of the Reynolds shear stress. Substantial drag reduction is achieved
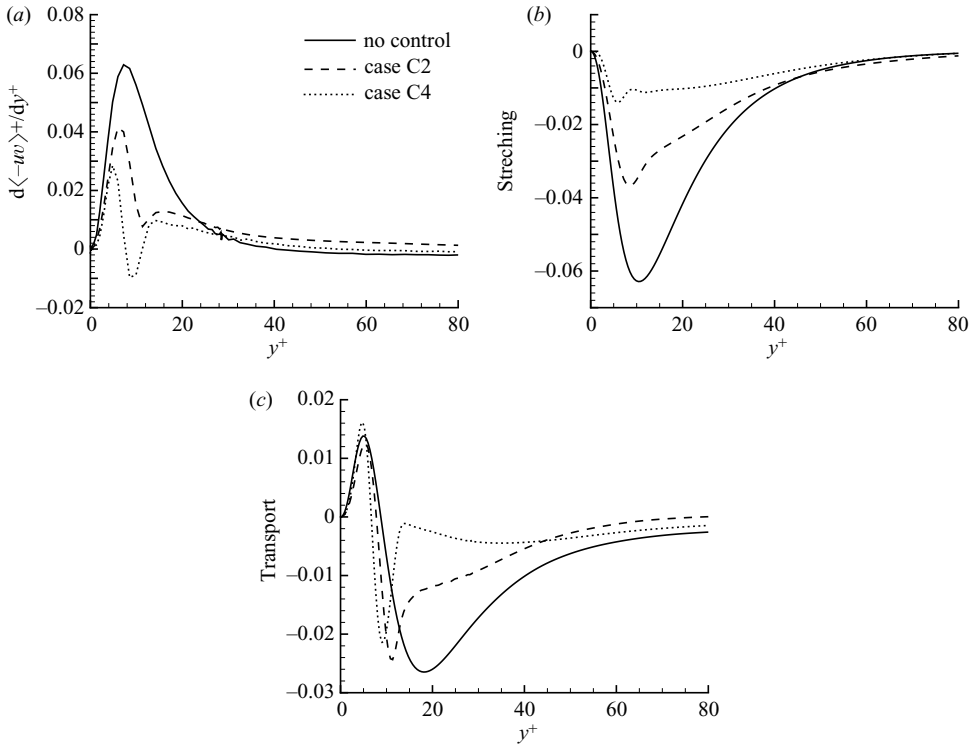
J. Xu, S. Dong, M. R. Maxey and G. E. Karniadakis

FIGURE 20. Profiles of (*a*) Reynolds stress gradient, (*b*) vortex stretching $\overline{u_3\omega_2}^+$, (*c*) vortex transport $\overline{u_2\omega_3}^+$: case C4, $I^+ = 0.36$; case C2, $I^+ = 0.27$; and base flow.

even for lower amplitudes. The streamwise forcing must be localized near the wall, preferably with $\lambda^+ < 13$–15. The dynamics of the mean shear layer are characterized by the Reynolds number Re_S. Below $Re_S \sim 120$, the turbulent Reynolds stresses are uniformly reduced. In the approximate range $Re_S = 120$–140, the shear layer gives rise to a local increase in the Reynolds stress at the wall and begins to create its own flow transition. For $Re_S > 140$, more fully three-dimensional flow disturbances grow locally at the shear layer, limiting further reductions in drag.

The same controlling force is also effective in reducing the stresses during the transition process from laminar to turbulent flow. To this end, we have simulated the transition process in a channel flow at $Re_\tau = 135$, starting from a laminar flow field. In figure 21, we plot the history of the pressure gradient for the controlled transition as well as the natural transition. In order to accommodate this transition, a small amount of noise was added initially to the laminar field. We see that during the transition there is an overshoot in the pressure drop (and correspondingly in the wall shear stress), which is substantially higher than the asymptotic mean value in the stationary state. However, the maximum peak in the controlled case is below the level of the turbulent wall shear stress for the uncontrolled case.

The practical implementation of this method of drag reduction poses obvious challenges. The first key issue is how to produce a retarding force within a distance from the wall corresponding to $(\lambda^+/2) < 10$. At high speeds (e.g. $20\,\mathrm{m\,s^{-1}}$), this physical distance is less than $10\,\mu\mathrm{m}$ for a turbulent flow in water. On the other hand, the force amplitudes used here are smaller by an order of magnitude than the force levels used in turbulence control via travelling waves in Du & Karniadakis (2000). Ideally, the
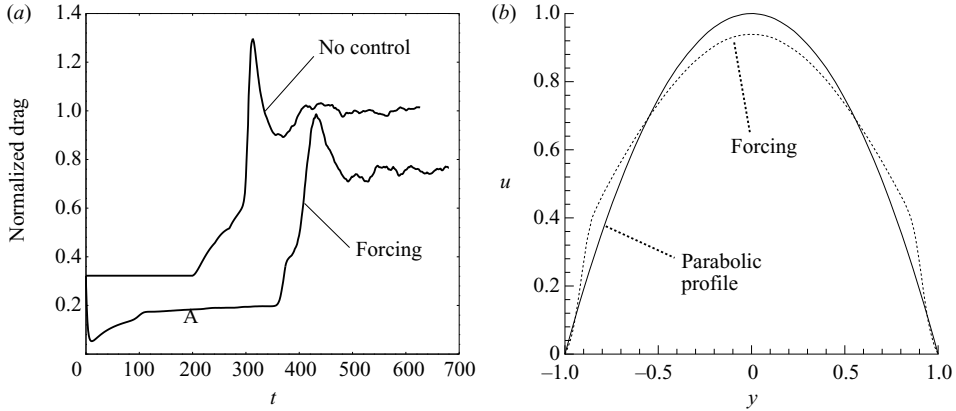
FIGURE 21. (*a*) Time history of pressure drop during transition in channel flow at $Re_\tau = 135$. All values are normalized with the value of the uncontrolled flow in the turbulent state, t is in convective units. (*b*) Streamwise velocity profile in the laminar state at time indicated by A.

excitation force should have its maximum retardation away from the wall at about $y^+ \approx 4$.

One approach might be to attempt to use an electromagnetic Lorentz force produced by a combination of wall-mounted magnetic tiles and near-wall electric currents in a conducting fluid such as seawater. Crawford & Karniadakis (1997) used Lorentz forces to produce a positive, as opposed to negative, streamwise forcing of the flow adjacent to the wall and observed an increase in the skin friction. The Lorentz force has its maximum at the wall and decays exponentially to zero with distance from the wall; therefore, it never reverses direction and thus the required pressure drop is larger than otherwise. The second key issue is then to induce a positive streamwise force away from the wall that counterbalances the retarding force in order to realize the maximum possible drag reduction.

An example of the effect of a Lorentz type of force distribution applied at each of the walls is

$$F_1(x_2) = -\rho I \{2 \exp(-h/\delta) \cosh(x_2/\delta) - \delta/h\}, \tag{5.1}$$

where locally near the wall the forcing decays on the length scale δ. This forcing exerts no net force on the flow and there is a small, uniform positive force to compensate for the negative force near each wall. Numerical results at $Re_\tau = 135$ show that for $I = 0.02$ ($I^+ = 0.073$) and $\delta/h = 0.017$ ($\delta^+ = 2.3$) there is about a 13 % reduction in the skin friction. For $\delta/h = 0.04$ ($\delta^+ = 5.4$), the skin friction is lower by 17 %. However, if we consider the balance (3.3), we find that $K_F = -0.164$ and -0.373, respectively, for the two cases. Thus, the direct effect of the forcing K_F accounts for the entire observed drag reduction for $\delta^+ = 2.3$, and for $\delta^+ = 5.4$ there is an increase in the turbulence. Indeed, the profile of the Reynolds shear stress shows just over a 20 % increase for this case. From this we may conclude that a Lorentz type of streamwise forcing of the flow will not be effective.

Finally, we comment on the power required to sustain the streamwise forcing and the flow through the channel. The negative streamwise forcing adjacent to the wall, in principle, extracts kinetic energy from the flow and the positive forcing further away from the wall supplies energy to the flow. Overall there is a net power input from the forcing that increases with the forcing amplitude. This will offset the power savings from the drag reduction and the reduction in the mean pressure gradient. At

$Re_\tau = 135$, with $\lambda^+ = 13.5$ and $I^+ = 0.073$ for case A1, the reduction in power required for the pressure gradient is 26 % while the net power required for the forcing is 10 % of the power input for the base flow, giving a total power savings of about 16 %. This drops to 10 %, however, if the kinetic energy is not extracted by the negative streamwise forcing. At $Re_\tau = 380$, case C4, there is an overall trade-off between the 70 % power savings from drag reduction and the power input for the forcing. This becomes a net increase in power of 17 % if the kinetic energy is not recovered from the flow by the negative portion of the streamwise force. At $Re_\tau = 633$, case D3, there is a net increase in the power required. These estimates do not take into account issues such as the efficiency of the force actuator.

These observations are not peculiar to this technique for drag reduction. Quadrio & Ricco (2004) report comparable results for drag reduction through spanwise oscillations of the walls. They give a detailed analysis of the efficiency and power savings. An intermittent forcing of the flow, or some other modification of the present technique, would be required to generate power savings at higher Reynolds numbers. The streamwise forcing is successful in reducing turbulence levels and this may be of value of itself for noise-reduction applications. Note what happens to the power supplied to the flow when the skin friction is reduced substantially. In both cases C4 and D3, the drag was reduced by 70 %, the Reynolds shear stresses were greatly reduced as was the overall turbulence production. A simple estimate shows that the direct viscous dissipation of kinetic energy by the mean flow increases with the forcing amplitude. Using (4.1) to calculate the additional viscous dissipation within the shear layer, the ratio of the added dissipation rate to the power supplied by the mean pressure gradient of the base flow $\rho u_\tau^2 U_B$ is $(3/8\pi^2)(I^+)^2(\lambda^+)^3(u_\tau/U_B)$. For case C4, this is approximately 60 % and 90 % for case D3.

While we may speculate about the practical issues of implementing this streamwise forcing technique for drag reduction, the results presented raise interesting fundamental issues about the interaction of an imposed near-wall shear layer with the turbulence.

REFERENCES

DEL ÁLAMO, J. & JIMÉNEZ, J. 2003 Spectra of the very large anisotropic scales in turbulent channels. *Phys. Fluids* **15**, L41–L44.

DEL ÁLAMO, J., JIMÉNEZ, J., ZANDONADE, P. & MOSER, R. 2004 Scaling of the energy spectra of turbulent channels. *J. Fluid Mech.* **500**, 135–144.

BECHERT, D. & BARTENWERFER, M. 1989 The viscous flow on surfaces with longitudinal ribs. *J. Fluid Mech.* **206**, 105.

BERGER, T., KIM, J., LEE, C. & LIM, J. 2000 Turbulent boundary layer control utilizing the Lorentz force. *Phys. Fluids* **12**, 631–649.

BUSHNELL, D. & MOORE, K. 1991 Drag reduction in nature. *Annu. Rev. Fluid Mech.* **23**, 65–79.

CHANG, Y., COLLIS, S. & RAMAKRISHNAN, S. 2002 Viscous effects in control of near-wall turbulence. *Phys. Fluids* **14**, 4069–4080.

CHOI, H., MOIN, P. & KIM, J. 1994 Active turbulence control for drag reduction in wall-bounded flows. *J. Fluid Mech.* **262**, 75–110.

CHOI, K.-S. 1989 Near-wall structure of a turbulent boundary layer with riblets. *J. Fluid Mech.* **208**, 417–458.

CRAWFORD, C. & KARNIADAKIS, G. 1997 Reynolds stress analysis of EMHD-controlled wall turbulence. Part I. Streamwise forcing. *Phys. Fluids* **9**, 788–806.

DEUTSCH, S., MOENY, M., FONTAINE, A. & PETRIE, H. 2003 Microbubble drag reduction in rough walled turbulent boundary layers. In *Proc. ASME, FEDSM2003-45647, 4th ASME/JSME Joint Fluids Engng Conf. Honolulu, Hawai, USA, July 6–11*.

DU, Y. & KARNIADAKIS, G. 2000 Suppressing wall turbulence by means of a transverse traveling wave. *Science* **288**, 1230–1234.

FIFE, P., WEI, T., KLEWICKI, J. & MCMURTY, P. 2005 Stress gradient balance layers and scale hierarchies in wall-bounded turbulent flows. *J. Fluid Mech.* **532**, 165–189.

FUKAGATA, K., IWAMOTO, K. & KASAGI, N. 2002 Contribution of Reynolds stress distribution to the skin friction in wall-bounded flows. *Phys. Fluids* **14**, L73–L76.

GAD-EL-HAK, M. 2000 *Flow Control*. Cambridge University Press.

HAMMOND, E., BEWLEY, T. & MOIN, P. 1998 Observed mechanisms for turbulence attenuation and enhancement in opposition-controlled wall-bounded flows. *Phys. Fluids* **10**, 2421–2423.

IWAMOTO, K., SUZUKI, Y. & KASAGI, N. 2002 Reynolds number effect on wall turbulence: toward effective feedback control. *Intl J. Heat Fluid Flow* **23**, 678–689.

JIMÉNEZ, J. & PINELLI, A. 1999 The autonomous cycle of near-wall turbulence. *J. Fluid Mech.* **389**, 335–359.

JIMÉNEZ, J., DEL ÁLAMO, J. & FLORES, O. 2004 The large scale dynamics of near-wall turbulence. *J. Fluid Mech.* **505**, 179–199.

KARNIADAKIS, G. & CHOI, K.-S. 2003 Mechanisms on transverse motions in turbulent wall flows. *Annu. Rev. Fluid Mech.* **35**, 45–62.

KARNIADAKIS, G. & SHERWIN, S. 2005 *Spectral/hp Element Methods for Computational Fluid Dynamics*, 2nd edn. Oxford University Press.

MAXEY, M., XU, J., DONG, S. & KARNIADAKIS, G. 2003 Simulation results for microbubbles and turbulent drag reduction. In *Proc. ASME, FEDSM2003-45638, 4th ASME/JSME Joint Fluids Engng Conf. Honolulu, Hawai, USA, July 6–11*.

MOSER, R., KIM, J. & MANSOUR, N. 1999 Direct numerical simulation of turbulent channel flow up to $Re_\tau = 590$. *Phys. Fluids* **11**, 943–945.

PHILLIPS, R., CASTANO, J. & STACE, J. 1998 Combined polymer and microbubble drag reduction. In *Proc. Intl Symp. on Seawater Drag Reduction, Newport RI*.

PTASINSKI, P., BOERSMA, B., NIEUWSTADT, F., HULSEN, M., VAN DEN BRULE, B. & HUNT, J. 2003 Turbulent channel flow near maximum drag reduction: simulations, experiments and mechanisms. *J. Fluid Mech.* **490**, 251–291.

QUADRIO, M. & RICCO, P. 2004 Critical assessment of turbulent drag reduction through spanwise wall oscillations. *J. Fluid Mech.* **521**, 251–271.

SREENIVASAN, K. 1989 The turbulent boundary layer. In *Proc. Frontiers in Experimental Fluid Mech.* (ed. M. Gad-el-Hak), pp. 159–209. Springer.

XU, J. 2005 High Reynolds number simulation and drag reduction techniques. PhD thesis, Brown University.

XU, J., MAXEY, M. & KARNIADAKIS, G. 2002 Numerical simulation of turbulent drag reduction using micro-bubbles. *J. Fluid Mech.* **468**, 271–281.